Nanoscale Advances

ROYAL SOCIETY OF CHEMISTRY

PAPER

View Article Online
View Journal | View Issue

Cite this: *Nanoscale Adv.*, 2025, 7, 1825

Graphene spatiotemporal reconfigurable intelligent surface (GSRIS) for terahertz polarization-state manipulation and holographic imaging

Tianyu Ma,[a] Liming Si, *[ab] Chenyang Dang,[a] Rong Niu,[a] Genhao Wu,[a] Xiue Bao,[a] Houjun Sun[ab] and Weiren Zhu *[c]

Received 9th September 2024
Accepted 3rd January 2025

DOI: 10.1039/d4na00750f

rsc.li/nanoscale-advances

The integration of 2D materials and metamaterials/metasurfaces presents an effective approach for the intelligent, real-time dynamic control of electromagnetic (EM) waves in the terahertz (THz) frequency range. Herein, we demonstrate a graphene spatiotemporal reconfigurable intelligent surface (GSRIS) for THz polarization-state manipulation, multi-beam generation and holographic imaging using EM theory and full-wave EM simulations. The chemical potential of graphene can be changed through time-varying modulation, such as field-programmable gate arrays (FPGAs), of the electric field or voltage. By dynamically controlling the spatiotemporal chemical potential of graphene, both the amplitude and phase of orthogonally polarized reflected waves can be simultaneously adjusted, enabling polarization state manipulation at different harmonics, multi-beam generation, and holographic imaging. As a proof of concept, a multifunctional GSRIS designed for 1.3 THz demonstrates polarization-state manipulation and multi-beam generation at the $+1^{st}$ order harmonic, as well as high-quality holographic imaging at the -1^{st} order harmonic. The presented GSRIS provides a novel approach for designing THz circuits and systems, which can exhibit various potential applications in imaging, sensing, beam control, and 6G wireless communications.

1. Introduction

Over the past decades, terahertz (THz) technology has attracted significant attention owing to its extensive applications in many fields such as biomedicine,[1] space exploration,[2] material characterization,[3] radio astronomy,[4] sensing,[5] imaging,[6] and 6G wireless communications.[7] Numerous intriguing phenomena have been studied within the THz frequency range, including the vibrational resonances of many molecules that fall within the THz and mid-IR frequency regions.[8] However, the generation, manipulation, and detection of THz waves remain significantly constrained by the lack of effective materials and technologies compared to the microwave and optical regimes, often referred to as the "THz gap".[9] As a result, the discovery and development of novel materials optimized for the THz frequency range are essential for advancing THz technology and applications. Two-dimensional (2D) materials, such as graphene, MXene and black phosphorus, offer a powerful platform for the generation, manipulation and detection of THz waves, particularly in active and reconfigurable applications.[10] Additionally, metamaterials and metasurfaces, composed of artificial subwavelength meta-atoms, provide opportunities to achieve unconventional electromagnetic (EM) properties not easily found in nature.[11–16] Therefore, the integration of 2D materials and metamaterials/metasurfaces presents an effective approach for intelligent real-time dynamic control of EM waves at THz frequencies.

Graphene is widely regarded as one of the most distinctive 2D materials for realizing tunable THz devices and applications.[17] It is well known that graphene is composed of a 2D honeycomb lattice structure of carbon atoms, exhibiting remarkable electronic, mechanical, and thermal properties.[18] The EM properties of graphene can be dynamically adjusted using electric fields, chemical doping, or mechanical folding methods. This tunability creates significant opportunities for innovations in THz filters, antennas, absorbers, modulators, as well as high-speed communications, imaging, and sensing.[19,20] However, it is worth noting that the properties of graphene are very sensitive to the type of edge atoms in a honeycomb lattice.[21] The type of edge atoms in graphene, whether armchair or

---

[a] *Beijing Key Laboratory of Millimeter Wave and Terahertz Technology, School of Integrated Circuits and Electronics, Beijing Institute of Technology, Beijing 100081, People's Republic of China. E-mail: lms@bit.edu.cn*

[b] *Tangshan Research Institute of Beijing Institute of Technology, Tangshan 063007, People's Republic of China*

[c] *Department of Electronic Engineering, Shanghai Jiao Tong University, Shanghai 200240, People's Republic of China. E-mail: weiren.zhu@sjtu.edu.cn*

zigzag, is determined on the basis of the orientation and structural configuration of graphene.[22] Variations in graphene's orientation and structure can give rise to new electronic states as well as transitions among insulating, conductive, and even superconductive behaviors.[23,24] Hence, we can argue that this phenomenon causes graphene to behave as an anisotropic and time-varying material, thereby enabling distinct space-time modulation in the THz range.

Reconfigurable intelligent surfaces (RISs) are a type of 2D metamaterial, specifically a metasurface, composed of periodic or aperiodic subwavelength meta-atoms.[25] They can effectively control EM waves, including reflection and transmission in terms of amplitude, phase and polarization.[26–31] In the microwave frequency range, a straightforward approach to implementing RISs is to use reconfigurable metasurfaces incorporating positive-intrinsic-negative (PIN) diodes,[32] varactor diodes,[33] transistors,[34] mechanical folding,[35] or micro-electromechanical system (MEMS) devices[36] within meta-atoms. In recent years, RISs have evolved from focusing solely on the spatial domain to incorporating the temporal domain, leading to the development of spatiotemporal RISs.[37,38] This advancement has revealed a variety of new phenomena, including harmonic control,[39] time-reversal symmetry for non-reciprocal transmission,[40,41] and real-time manipulation of multiple polarization states.[42] Additionally, advancements in dynamic metasurfaces have demonstrated promising results in controlling THz waves. For instance, tunable metasurfaces based on phase-change materials or graphene have been shown to enable beam steering,[43] polarization conversion,[44] and broadband absorption.[45] Spatiotemporal RISs are considered effectively applicable in various areas of microwave technology, such as beam steering, holographic imaging, real-time radar detection, wireless communication, and unmanned aerial vehicles (UAVs).[46,47] Although advanced THz systems with precise real-time control are highly desirable,[48] implementing spatiotemporal RISs at THz frequencies remains a significant challenge due to material limitations and integration issues.

In this work, we present a configuration for implementing spatiotemporal RISs at THz frequencies through the integration of graphene and metasurfaces, which is herein called a "graphene spatiotemporal reconfigurable intelligent surface" (GSRIS). The proposed GSRIS, operating in the THz frequency range, significantly enhances its versatility and performance in real-time applications. We theoretically calculate and numerically analyze the performance of the GSRIS using EM theory and full-wave EM simulations, focusing on THz polarization state manipulation, multi-beam generation, and holographic imaging. When illuminated with light of specific frequency and polarization states, the GSRIS can be programmatically controlled to produce variable polarization and spatially multiplexed beams through harmonic frequency conversion. By altering time-varying external polarization voltage to control the chemical potential of graphene, such as through a, FPGAs, independent modulation of each unit can be achieved. As verification, the designed GSRIS successfully generates one-to-four beam channels with different polarization states at the +1st order harmonic, with each channel exhibiting different scattering modes. In addition, THz holographic imaging is realized at the -1st order harmonic, demonstrating high-resolution imaging capabilities. The proposed GSRIS enhances the potential of metasurfaces in THz applications, including imaging, sensing, beam control, and 6G wireless communications.

2. Materials and methods

Fig. 1 shows the designed GSRIS simultaneously generating multiple beams with different polarization states. The unit structure that supports independent control of each meta-atom's x and y polarizations is depicted in the figure. The proposed GSRIS unit is composed of multiple layers of different materials arranged from top to bottom. The combination of the top orthogonal graphene strips enables independent control over orthogonal EM responses, with the length and width of the graphene sheets being $l_g = 18$ μm and $w = 3.9$ μm, respectively. Below this is a layer of Al_2O_3 and SiO_2, each with a thickness of $t_s = 65$ nm. The relative permittivity of Al_2O_3 is $\varepsilon_r, A_l = 9.9$. There is a quartz substrate with a thickness of $h = 27$ μm (with $\varepsilon_r = 3.75$ and $\tan\delta = 0.0184$). The metal ground layer terminates the metasurface to avoid energy transmission, thereby creating a reflective digital metasurface. The electrical conductivity of the metal is $\sigma = 4.56 \times 10^7$. Full-wave simulations of the co-polarized reflection coefficient of the GSRIS were conducted using commercial CST Microwave Studio 2020 software. Periodic boundary conditions were applied in the x and y directions to simulate an infinite array, while open boundary conditions were applied in the z direction.

Considering the $M \times N$ spatiotemporal encoded GSRIS, graphene is chosen as the tunable material. Because of its high sensitivity to external gate bias, graphene can dynamically control terahertz frequency EM waves with a fast response time. Furthermore, owing to its single-layer structure, graphene can be modeled as an infinitely thin surface with a specific surface conductivity (σ_s). The surface conductivity of graphene is the sum of the intra-band (σ_{intra}) and inter-band (σ_{inter}) conductivities, which is defined as follows using the Kubo formula:[49]

$$\sigma_s = \sigma_{\text{intra}}\omega,\mu_c,\Gamma,T + \sigma_{\text{inter}}\omega,\mu_c,\Gamma,T \tag{1}$$

$$\sigma_{\text{intra}}\omega, \mu_c, \Gamma, T = \frac{-je^2k_BT}{\pi\hbar^2(\omega - j2\Gamma)}\left(\frac{\mu_c}{k_BT} + 2\ln\left(e^{-\mu_c k_B T} + 1\right)\right) \tag{2}$$

$$\sigma_{\text{inter}}\omega, \mu_c, \Gamma, T = -j\frac{e^2}{4\pi\hbar}\ln\left(\frac{2|\mu_c| - (\omega - j2\Gamma)\hbar}{2|\mu_c| + (\omega - j2\Gamma)\hbar}\right) \tag{3}$$

$$\tau = \frac{\mu\mu_c}{evf^2} \tag{4}$$

where e, h, k_B, T and μ_c are the electron charge, reduced Planck's constant, Boltzmann constant, temperature and chemical potential (*i.e.* Fermi energy E_F), respectively. The parameter $\Gamma = 1/2\tau$ (where τ is relaxation time) represents

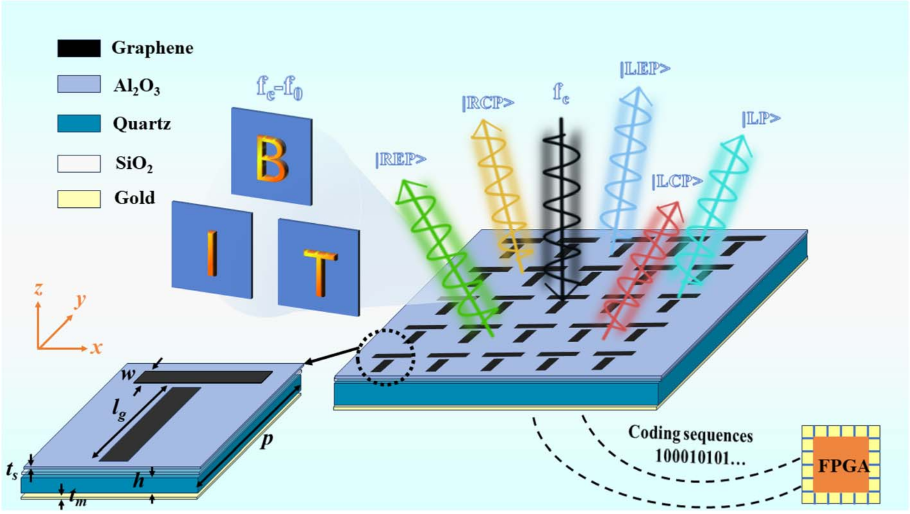

Fig. 1 Schematic of the designed GSRIS for THz polarization-state manipulation.

collision frequency. Relaxation time (τ) and temperature (T) are assumed to be 1 ps and 300 K, respectively. In eqn (4) $\mu = 10^4\ \mathrm{cm}^2\ \mathrm{V}^{-1}\ \mathrm{s}^{-1}$ is the carrier mobility of graphene, and $v_f = 10^6\,\dfrac{m}{s}$ is Fermi velocity. Therefore, in the terahertz region, graphene is well described by Drude-like surface conductivity, and its sheet conductivity can be controlled by chemical potential (μ_c). A design for an anisotropic GSRIS that supports independent control of the x- and y-polarized responses of each unit is implemented.

Co-polarized reflection simulations for x- and y-polarized incidence are presented in Fig. 2. Herein, the chemical potentials in the x- and y-polarization directions are denoted as (μ_x,μ_y), respectively. Independent control of reflection coefficients for x- and y-polarized waves could be achieved by adjusting the chemical potentials μ_x and μ_y applied to the graphene strips along the x- and y-axes. Fig. 2 depicts amplitude and phase representations for two different working states based on the chemical potential combinations. For example, (0, 1) represents $\mu_x = 0$ eV and $\mu_y = 1$ eV, and (0, 0.5) represents $\mu_x = 0$ eV and $\mu_y = 0.5$ eV. As shown in Fig. 2, when either μ_x or μ_y is fixed, corresponding polarization amplitude and phase remain consistent, while the chemical potential of the altered polarization can maintain a phase difference of 180° ± 20° in the range of 1.2–1.7 THz. These results demonstrate that the designed unit structure enables independent control of x and y polarizations, with no mutual interference between them. Herein, we selected 1.3 THz as the working frequency (f_c). Meanwhile, in our design, by regulating the chemical potential, a phase difference of 180° can be achieved. At positions (0, 0.5) or (0.5, 0), the phase is 180°, while at positions (0, 1) h or (1, 0), the phase is 0°. Here, the code "1" corresponds to a 180° phase, and the code "0" corresponds to a 0° phase.

To further explore the polarization manipulation mechanism of the proposed cross structure, the surface current distribution of the unit cell in two operating states was simulated. As shown in Fig. 3, these surface current maps represent the unit at 1.3 THz for two different graphene chemical potentials. We examined two different cases of applying chemical potential to graphene, with 1 eV applied to graphene in both the x and y directions. It can be observed that when chemical potential is varied in either the x or y direction, current density in the same polarization direction on the side where the chemical potential is applied is significantly higher than in the other direction. Therefore, the designed GSRIS unit can independently control the reflection of x and y polarized light with minimal polarization crosstalk.

3. Results and discussion

3.1. Polarization-state manipulation at the +1$^{\mathrm{st}}$ order harmonic

To achieve spatiotemporal modulation of multi-beam polarization control at the +1$^{\mathrm{st}}$ order harmonic, a two-step process is necessary. The initial step entails the computation of the theoretical phase and amplitude patterns that will produce the desired polarization state of the targeted beam. Subsequently, in the second step, spatiotemporal coding techniques are employed to implement the calculated phase and amplitude distribution. This step utilizes specific optical components or systems that can modulate the beam's spatial and temporal properties. By doing so, phase and amplitude variations can be precisely controlled to generate the desired multi-beam polarization control. By integrating these two steps, a comprehensive approach is established to generate spatiotemporally modulated multi-beam polarization control at the +1$^{\mathrm{st}}$ order harmonic.

First, we assume that modulation frequency is much lower than the frequency of EM waves. Spatiotemporal encoding theory is derived using a physical optics model approximation, where mutual coupling between encoding units is temporarily

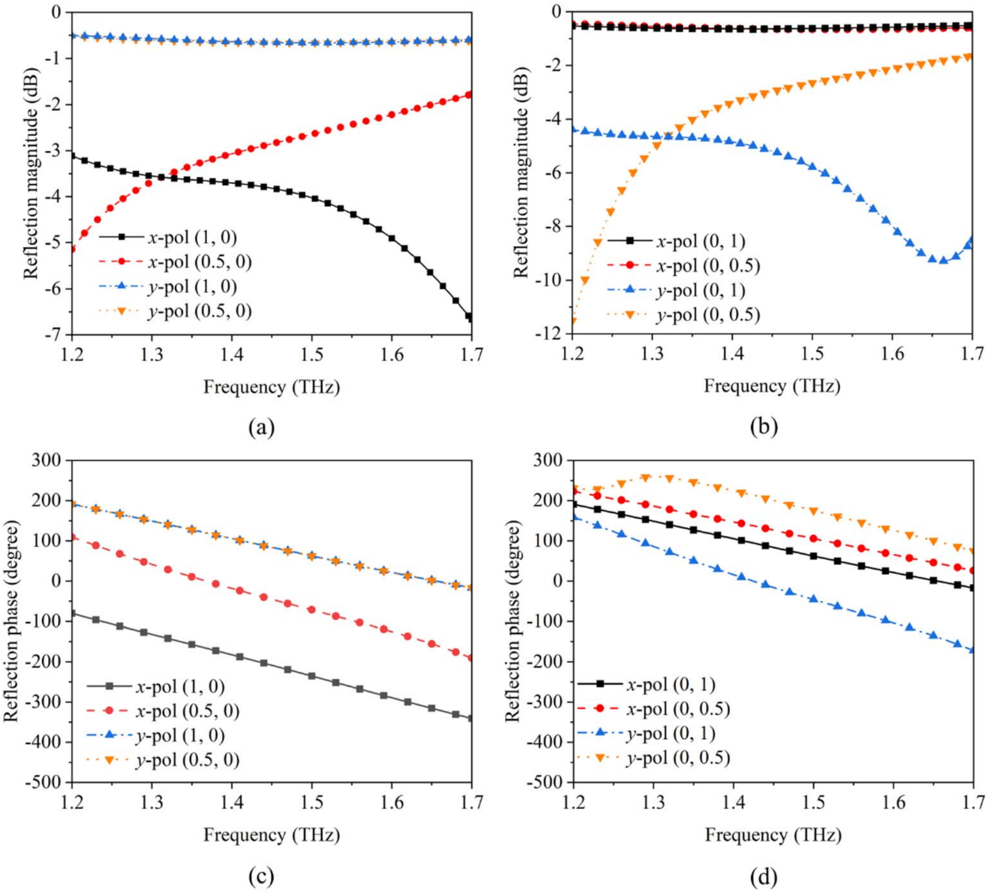

Fig. 2 Simulation performance of the unit: (a) reflection amplitude of x-polarization and y-polarization when changing only μ_x. (b) Reflection amplitude of x-polarization and y-polarization when changing only μ_y. (c) Reflection phase of x-polarization and y-polarization when changing only μ_x. (d) Reflection phase of x-polarization and y-polarization when changing only μ_y.

neglected in the approximate model. Modulation frequency in time is much smaller than the frequency of EM waves. Assuming that the required light beam is generated by a GSRIS consisting of $M \times N$ meta-atoms and that it supports independent control of x- and y-polarized responses for each meta-atom, the far-field electric field can be represented as the collective result of all meta-atoms:

$$E(\theta,\phi) = \sum_{n=1}^{N}\sum_{m=1}^{M} A_x(m,n)\exp\left\{i\left[\varphi_x(m,n) + \left(m-\frac{1}{2}\right)k_D \sin\theta\cos\phi + \left(n-\frac{1}{2}\right)k_D\sin\theta\sin\varphi\right]\right\}e_x$$
$$+\sum_{n=1}^{N}\sum_{m=1}^{M} A_y(m,n)\exp\left\{i\left[\varphi_y(m,n) + \left(m-\frac{1}{2}\right)k_D \sin\theta\cos\phi + \left(n-\frac{1}{2}\right)k_D \sin\theta\sin\phi\right]\right\}e_y \quad (5)$$

where θ and ϕ represent the elevation and azimuth angles, respectively. $A_x(m,n)$, $A_y(m,n)$, $\varphi_x(m,n)$, and $\varphi_y(m,n)$ denote the x- and y-polarization amplitude and phase responses of the meta-atoms located in the m-th column and n-th row, respectively. Here, D stands for the period of the meta-atom array, and $k = 2\pi/\lambda_c$ is the wave number in free space.

By modulating phase discontinuities and orthogonally polarized reflective fields, a single beam with a specified polarization state can be achieved. According to Snell's law, the addition of phase gradients ($\mathrm{d}\Phi/\mathrm{d}l$) determines the scattering direction of the beam. To achieve the desired polarization state, the orthogonal polarized electric field $E_{(\chi,\psi)}$ should contain x-polarized and y-polarized components:[50]

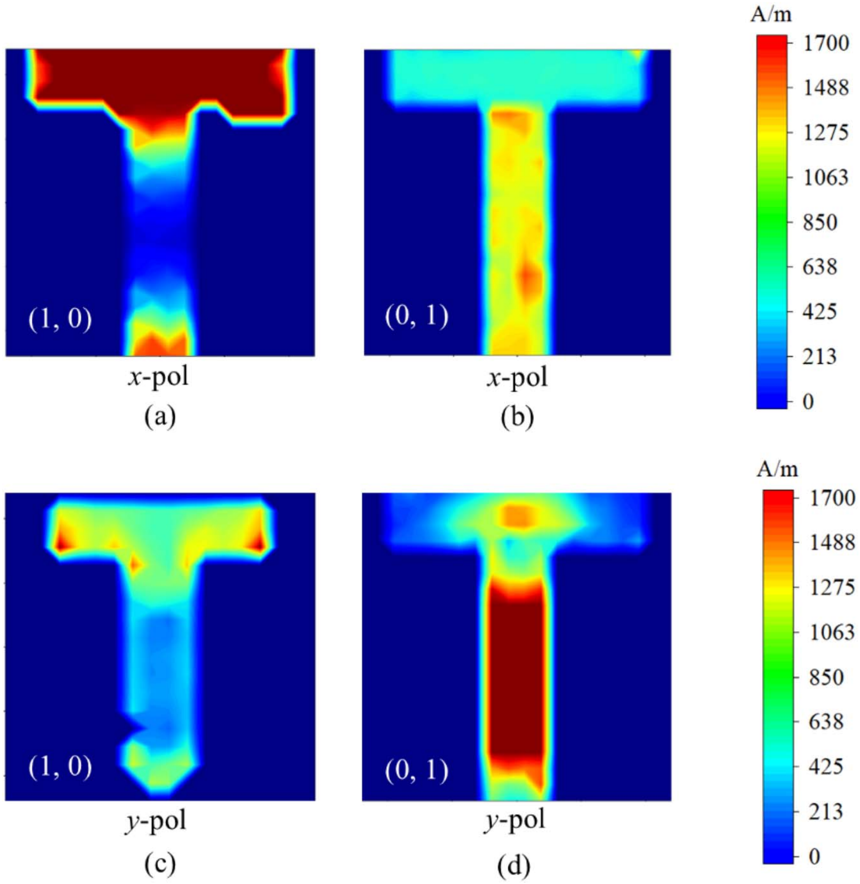

Fig. 3 (a and b) Graphene surface current distributions for the units (1,0) and (0,1) under x-polarization. (c and d) Graphene surface current distributions for the units (1,0) and (0,1) under y-polarization.

$$E_{\chi,\psi} = \left(E_x E_y\right)\begin{pmatrix} e_x \\ e_y \end{pmatrix} \tag{6}$$

where χ represents the ellipticity angle, and ψ represents the orientation angle.

$$E_x = \cos\psi\sin\chi - j\sin\psi\cos\chi$$

$$E_y = \sin\psi\cos\chi - j\cos\psi\sin\chi$$

The matrices E_x and E_y represent the Jones matrices of the polarization state of any point light in the Poincaré sphere, which are based on the basis vectors of linear polarization in the x and y directions, respectively. The polarization state of the light beam is controlled by E_x and E_y. Therefore, we set the incident light to be vertically incident on the GSRIS. This configuration allows us to obtain the theoretical phase and distribution of the light beam with the specified polarization state. By combining eqn (5) and (6), it is possible to achieve a single beam with the desired polarization state by adjusting the amplitude and phase responses of each meta-atom.

$$\frac{A_y e^{j\varphi_y}}{A_y e^{j\varphi_y}} = \frac{E_y^r E_x^i}{E_y^i E_x^r} \tag{7}$$

where $\begin{cases} E_x^i = \cos\psi^i\cos\chi^i - j\sin\psi^i\sin\chi^i \\ E_y^i = \sin\psi^i\cos\chi^i - j\cos\psi^i\sin\chi^i \\ E_x^r = \cos\psi^r\cos\chi^r - j\sin\psi^r\sin\chi^r \\ E_y^r = \sin\psi^r\cos\chi^r - j\cos\psi^r\sin\chi^r \end{cases}$

Here, we define $|\mathrm{LP}\rangle|\mathrm{LP}\rangle|\mathrm{LP}\rangle$ as linearly polarized, $|\mathrm{RCP}\rangle$ as right-handed circularly polarized, $|\mathrm{LEP}\rangle$ as left-handed elliptically polarized, and $|\mathrm{REP}\rangle$ as right-handed elliptically polarized. To verify the ability of the designed GSRIS to generate patterns in different polarization directions, we conducted theoretical calculation for a 10 × 10 array. Our goal, as shown in Fig. 4, was to generate four beams with distinct polarization states and deflection directions. Each of these beams has the following properties: $|\mathrm{LP}\ 52°\rangle$ with $(\theta,\phi) = (0°, 36°)$, as shown in Fig. 4(a); $|\mathrm{LEP}\rangle$ with $(\chi,\psi) = (30°, 25°)$ and $(\theta,\phi) = (180°, -36°)$, as shown in Fig. 4(c); $|\mathrm{RCP}\rangle$ with $(\theta,\phi) = (90°, -16°)$, as shown in Fig. 4(b); and $|\mathrm{REP}\rangle$ with $(\chi,\psi) = (-12°, 57°)$ and $(\theta,\phi) = (270°, 16°)$, as shown in Fig. 4(d). In this context, χ and ψ determine the polarization state of the beam, whereas θ and ϕ determine the deflection angle of the beam. In this case, using a linearly polarized (LP) light beam as an example, the EM properties of each meta-atom are designed with $A_y/A_x = \tan(52°)$, and the phase difference between the x and y directions is 0, *i.e.*,$\varphi_x = \varphi_y$. Additionally, 0 achieve the desired beam deflection angle of 36°, an additional phase gradient of $\mathrm{d}\Phi/\mathrm{d}x = 1.22\pi/\lambda_c$ is determined using the generalized Snell's reflection law.

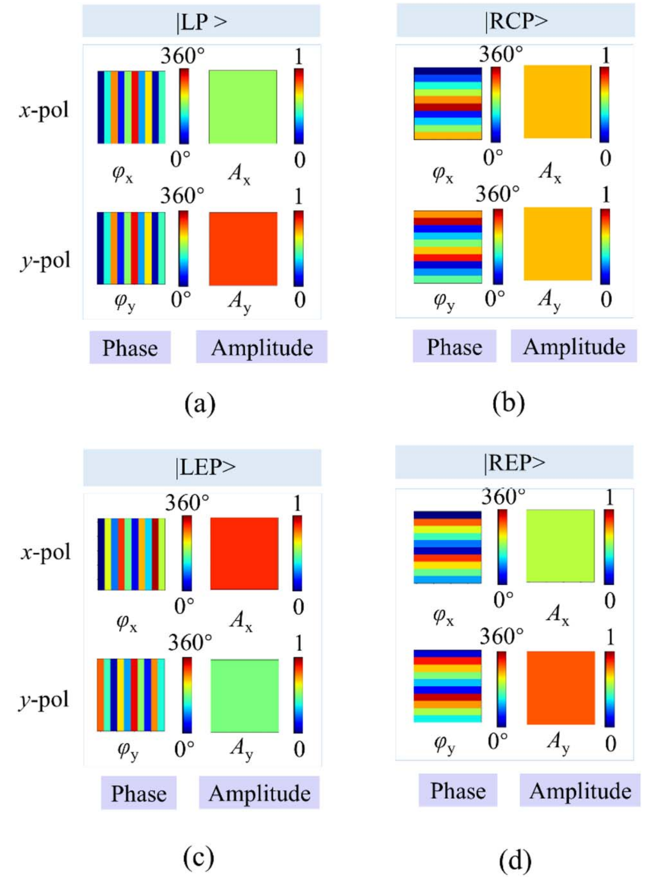

Fig. 4 Amplitude-phase distribution of x-pol and y-pol under different polarization states: (a) linear polarization. (b) Right circular polarization. (c) Left elliptical polarization. (d) Right elliptical polarization.

The final amplitude and phase distribution of the single beam with a 36° deflection angle and a linear polarization state of 52° are obtained. Here, we assess the polarization state by the amplitude ratio and phase difference between the x-polarized and y-polarized components. Therefore, the solution is not unique. Each pattern is accompanied by the normalized intensity of different polarization states. Selecting "1111" provides a far-field normalized scattering pattern, along with the corresponding time encoding for x-polarization and y-polarization and lists the polarization states present in that channel. For beam deflection in this pattern, phase gradients of $\mathrm{d}\phi/\mathrm{d}x = \pm 1.22\pi/\lambda_c$ and $\mathrm{d}\phi/\mathrm{d}y = \pm 0.63\pi/\lambda_c$ were pre-designed. To simplify the analysis of polarized beams, normalize the amplitude distribution, ensure energy conservation, and facilitate mathematical processing, we assume the spatial amplitude distribution as $A_y{}^2 + A_x{}^2 = 1$. LEP represents a beam with a polarization state of ($\chi = 30°$, $\psi = 25°$) and a deflection angle of −36°. RCP represents a polarized beam with a deflection angle of −16°. REP represents a polarized beam with a polarization state of ($\chi = -12°$, $\psi = 57°$) and a deflection angle of 16°.

Next, utilizing the superposition principle, the respective complex amplitudes and phase distributions will be added to create multiple radiation beams with specific polarization states. The overall amplitude and phase distribution for simultaneously generating multiple polarized beams can be calculated as follows:

$$\Gamma_x = \boldsymbol{\Gamma}_x \boldsymbol{P} \tag{8}$$

$$\Gamma_y = \boldsymbol{\Gamma}_y \boldsymbol{P} \tag{9}$$

where Γ is an $M \times N$ matrix representing the reflection coefficients of each meta-atom. The vectors $\boldsymbol{\Gamma}_x = [\Gamma_x{}^1, \Gamma_x{}^2, \ldots, \Gamma_x{}^q]$ and $\boldsymbol{\Gamma}_y = [\Gamma_y{}^1, \Gamma_y{}^2, \ldots, \Gamma_y{}^q]$ represent the polarization components of the q-th beam along the x and y directions. The superscript q denotes the q-th beam, while the subscript x/y represents the x/y polarization component. The parameter p_q signifies the weight of the q-th beam, which is used to adjust the energy distribution of each beam. The vector $\mathbf{P} = [p_1, p_2, \ldots p_q]^{\mathrm{T}}$ contains the weights for all the beams. Ideally, if each beam is set to equal weight value of $\mathbf{P}$, multiple beams with the same maximum intensity can be generated. By applying different weights to distinguish between different beams, it is possible to observe multiple beams with unequal intensities.

To differentiate between various beam patterns, the binary code "1" signifies the generation of a beam with a specific predefined polarization, while "0" indicates the absence of beam generation. For instance, the code "1111" corresponds to the generation of four beams, whereas "0000" signifies that no beams are generated. The sequence of binary codes, read from right to left, delineates beams characterized by specific polarization states: $|\mathrm{LP}\rangle$, $|\mathrm{LEP}\rangle$, $|\mathrm{RCP}\rangle$, and $|\mathrm{REP}\rangle$. Fig. 5 illustrates a transition from the generation of a single polarized beam to the creation of three beams, showcasing the intensities and polarization states across all beams. Fig. 5(a) shows the scattering pattern of a single beam channel "0001", "0010", "1000", and "0100" as well as their corresponding polarization intensities. Fig. 5(b) shows the scattering pattern of double beam channels "1010", "0101", "0011", and "1100" as well as their corresponding polarization intensities. Fig. 5(c) shows the scattering pattern of triple beam channels "0111", "1011", "1101", and "1110" and their corresponding polarization intensities. We can observe that the intensity of the polarization states of the different channels matches the target, demonstrating the feasibility of the designed method.

The second step involves achieving the desired amplitude and phase distributions within the polarization channels through temporal signals, enabling free modulation of both. The time-modulated reflection coefficient of the (m,n)-th encoded unit $R_{mn}(t)$ is a periodic function of time, defined as a linear combination of a series of shifted pulse functions within one period:[38]

$$R_{mn}(t) = \sum_{i=1}^{L} R(t) U_{mn}^{i}(t) \tag{10}$$

where $U_{mn}^{i}(t)$ is a periodic pulse function with a modulation period of T_0. The expression is as follows:

$$U_{mn}^{i}(t) = \begin{cases} 1, (iT_0/L \le t \le (i+1)T_0/L) \\ 0, \text{else} \end{cases} \tag{11}$$

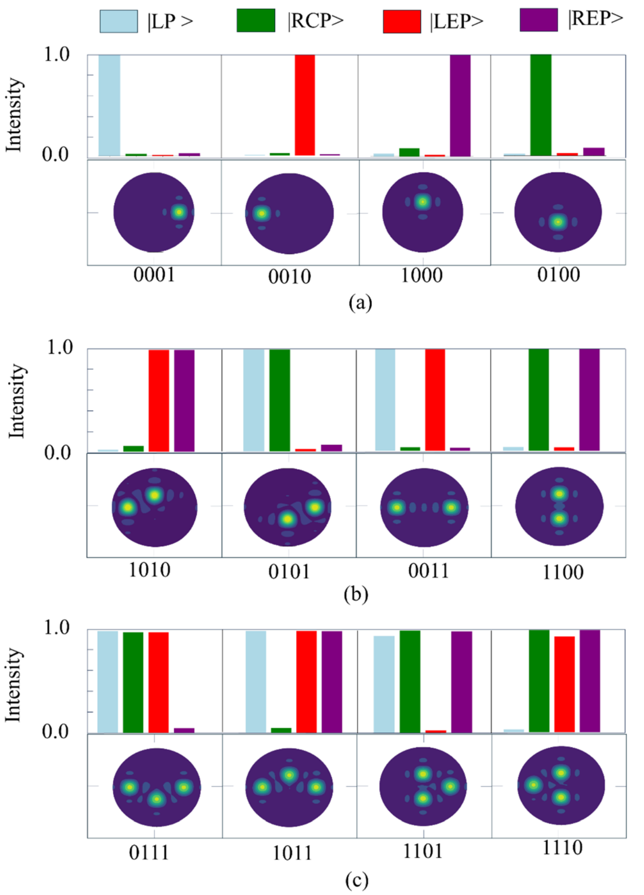

Fig. 5 The intensity of various polarization states in different channels. (a) Polarization intensities in the single beam channels "0001", "0010", "1000", and "0100". (b) Polarization intensities in the double beam channels "1010", "0101", "0011", and "1100". (c) Polarization intensities in the triple beam channels "0111", "1011", "1101", and "1110".

where $R(t) = A_{mn}^{i}e^{j\varphi_{mn}^{i}}$, $R(t)$ represents the reflection coefficient of the (m,n)-th coding unit within the time interval $iT_0/L \leq t \leq (i+1)T_0/L$, with A_{mn}^{i} and φ_{mn}^{i} denoting the amplitude and phase of reflection coefficient, respectively. By performing a Fourier expansion on eqn (11), the Fourier coefficients of $U_{mn}^{i}(t)$ are obtained. Substituting these coefficients into eqn (10) yields the Fourier series for $R_{mn}(t)$. Specifically, by altering the properties of the GSRIS, the reflection coefficient $R_{mn}(t)$ of the meta-atoms can be decomposed into a sum of harmonic components based on Fourier series expansion:

$$R_{mn}(t) = \sum_{s=-\infty}^{+\infty} a_s e^{j2\pi s f_0 t} \tag{12}$$

where $f_0 = 1/T_0$ represents modulation frequency, s denotes the order of harmonic frequency, and the Fourier coefficient a_s is given by the following equation:

$$a_s = \sum_{i=1}^{L} \frac{R_i}{L} \sin^{-1}\left(\frac{\pi s}{L}\right) \exp\left[\frac{-j\pi s(2i-1)}{L}\right] \tag{13}$$

where L denotes the length of the time-varying signal during a designated time period. Based on eqn (12) and (13), a solitary modulation signal induces a specific effective reflection performance. By iterating over each conceivable time-varying modulation signal of a predetermined length, a comprehensive database of all possible effective reflections is compiled. This database encompasses all normalized effective reflections at the first harmonic frequency ($s = 1$) generated by the modulating signal with $L = 12$. It has been discovered that time-varying modulation imbues the reflection coefficients with supplementary amplitude modulation and phase delays, thereby facilitating a versatile amalgamation of phase and amplitude responses. Utilizing this framework, any desired anisotropy of a super glossy surface can be modeled by judiciously selecting signals from the database to achieve the targeted complex amplitudes $A_x \exp(j\varphi_x)$ and $A_y \exp(j\varphi_y)$.

As illustrated in Fig. 6, the complex amplitude and phase distributions of the polarization states for the four beams are determined, leading to the retrieval of corresponding codes from the database. Subsequently, necessary time code sequences for application are generated. The time encoding of the amplitude phase corresponds to the x-polarization for this pattern. Fig. 6(a) and (b) illustrate the temporal encoding of amplitude and phase distributions corresponding to "1111" for x-polarization and y-polarization respectively. Fig. 6(c) and (d) display the normalized intensities of the four different polarization states and the polarization states across the four channels. It can be observed that the intensities of the four polarization states are almost identical. Fig. 6(e) and (f) present the generated 2D far-field patterns for the four spatial beams as well as normalized scattering patterns in the xoz and yoz planes. It can be observed that the four beams are reflected at ±36° and ±16° directions, fulfilling the design requirements. Moreover, the polarization state intensities of the designed beams align with the target and fulfills the requirements.

3.2. THz hologram images at the -1$^{\text{st}}$ order harmonic

The spatiotemporal metasurface has the capability to control amplitude and phase at different harmonic frequencies. Here, near-field holographic imaging achieved at the -1$^{\text{st}}$ order harmonic supports this functionality. Achieving holographic imaging at the -1$^{\text{st}}$ order harmonic involves a systematic approach. Initially, the crucial step is to determine and obtain the necessary amplitude and phase distribution, which are essential for accurate imaging. Subsequently, in the second step, the modulation of amplitude and phase at the -1$^{\text{st}}$ order harmonic is achieved through the application of spatiotemporal coding techniques. This ensures that the results align with the theoretical calculations obtained in the initial step, thereby enabling precise holographic imaging.

Based on the Huygens–Fresnel imaging principle, the field $U_i(x,y,0)$ on the GSRIS plane can be approximately solved using the given field of a two-dimensional virtual object. This results in the field $U(x,y,d)$ on the imaging plane at $U_i(x,y,d)$, which can be expressed as:

$$U_i(x,\gamma,0) = \frac{L_x L_\gamma}{MN} \sum_{a=1}^{M} \sum_{b=1}^{N} \frac{d(1-jkR)e^{jkR}}{2\pi R^3} U(x,y,d) \tag{14}$$

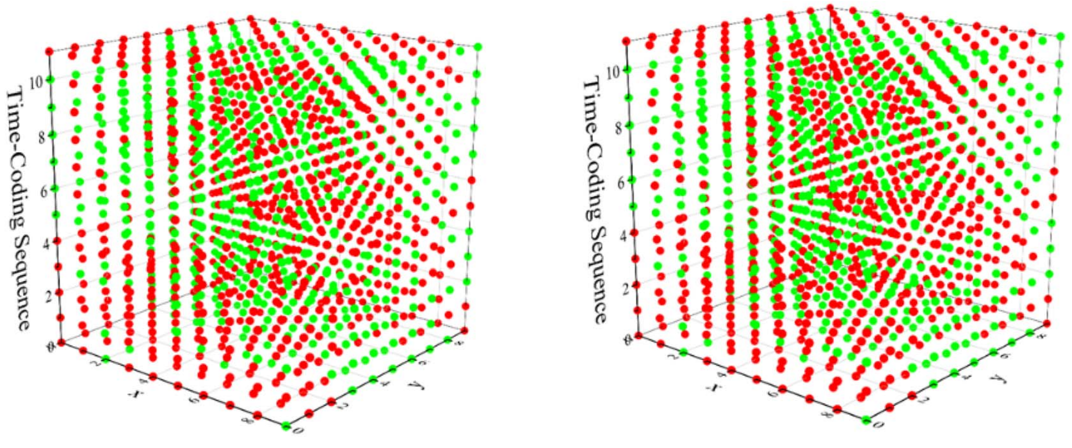

x-pol-time coding y-pol-time coding

(a) (b)

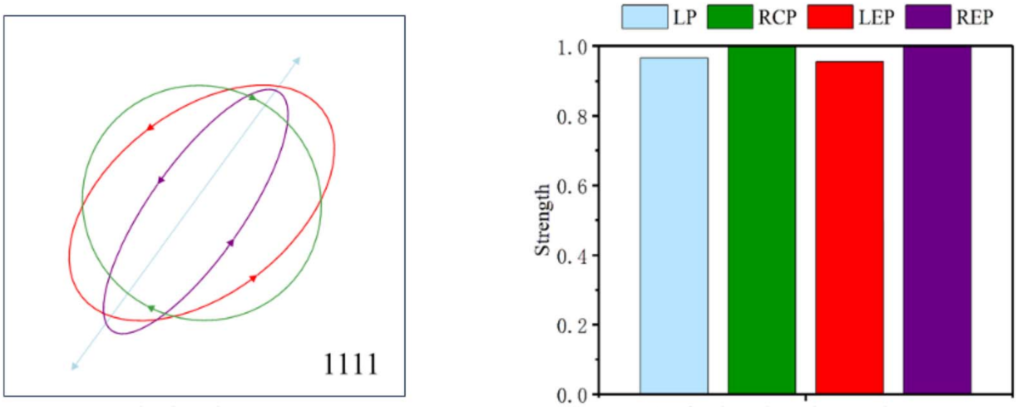

Polarization state Polarization intensity

(c) (d)

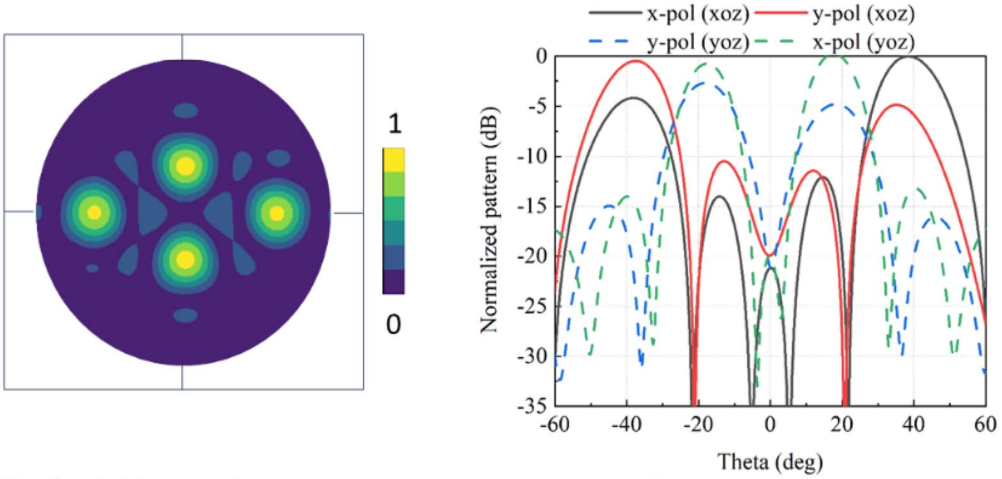

2D far-field scattering pattern Normalized scattering patterns

(e) (f)

Fig. 6 Description of the four-beam channel. (a) Four-beam spatiotemporal coding state in *x*-pol. (b) Four-beam space-time coding state in *y*-pol. (c) Four polarization state types. (d) Four polarization intensities. (e) 2D far-field scattering pattern. (f) Normalized scattering patterns.

where $R=\sqrt{[x-(a-0.5)L_x/M]^2+[\gamma-(b-0.5)L_\gamma/N]^2+d^2}$ and k is wavenumber, $U(x,y,d)=U((a-0.5)L_x/M,(b-0.5)L_\gamma/N,d)$. In eqn (14), the imaging surface with dimensions $L_x\times L_y$ is discretized into $M\times N$ pixels. Conversely, $U(x,y,d)$ can also be calculated based on $U_i(x,y,0)$:

$$U(x,y,d)=\frac{L_xL_\gamma}{MN}\sum_{a=1}^{M}\sum_{b=1}^{N}\frac{d(1+jkR)\mathrm{e}^{-jkR}}{2\pi R^3}U_i(x,y,0) \tag{15}$$

where $U_i(x,y,0)=U_i((a-0.5)L_x/M,(b-0.5)L_\gamma/N,0)$.

Next, the GS algorithm can obtain the required amplitude and phase on the GSRIS array by alternately solving eqn (14) and (15). Specifically, assuming that the designed GSRIS is a perfect reflective array, its reflection amplitude is always set to 0.6. An initial random phase distribution of the array is given. Using eqn (15), the field $U(x,y,d)$ on the imaging plane is calculated. The amplitude of $U(x,y,d)$ is then replaced with the desired amplitude on the imaging plane, and the resulting $U(x,y,d)$ is inserted into eqn (14) to solve the field $U_i(x,y,0)$ on the GSRIS array. The amplitude of $U_i(x,y,0)$ is then replaced with the ideal reflection amplitude of −1.

An initial random phase distribution is assigned to the array. Using eqn (15), the field $U(x,y,d)$ on the imaging plane is calculated. The amplitude of $U(x,y,d)$ is then substituted with the desired amplitude on the imaging plane. This updated field $U(x,y,d)$ is then inserted into eqn (14) to determine the field $U_i(x,y,0)$ on the GSRIS array. Finally, the amplitude of $U_i(x,y,0)$ is replaced with the ideal reflection amplitude of 0.6.

This process is repeated until the calculated image closely matches the desired image on the imaging plane. Here, we perform a theoretical validation for a 100 × 100 array, with the distance d between the metasurface array and the imaging plane set to 4 mm. As shown in Fig. 7(a) and (b), a time-modulated signal is selected with $L=12$ to ensure that the desired phase and amplitude levels are achieved. Next, using eqn (14) and (15), the complex amplitude and phase distributions at the -1st harmonic are obtained, as illustrated in Fig. 7(c). The corresponding spatiotemporal coding is derived from this amplitude and phase distribution on the holographic GSRIS array, allowing the achievement of the desired amplitude and phase distribution by applying an appropriate spatiotemporal coding.

Fig. 8 presents the simulated holograms at the -1st order harmonic on an imaging plane, with a central working frequency of 1.3 THz. The phase distribution for the holographic imaging of the letters ("B", "I", and "T") and their corresponding imaging results are shown in Fig. 8. To evaluate the quality of the holographic image, the signal-to-noise ratio (SNR) can be calculated as $\mathrm{SNR}=10\log_{10}(\mathrm{S/N})$, where S and N are the sums of the electric field amplitudes in the image region and the remaining region, respectively. The SNRs of the holographic images for the letters "B", "I", and "T" are 7.65 dB, 7.55 dB, and

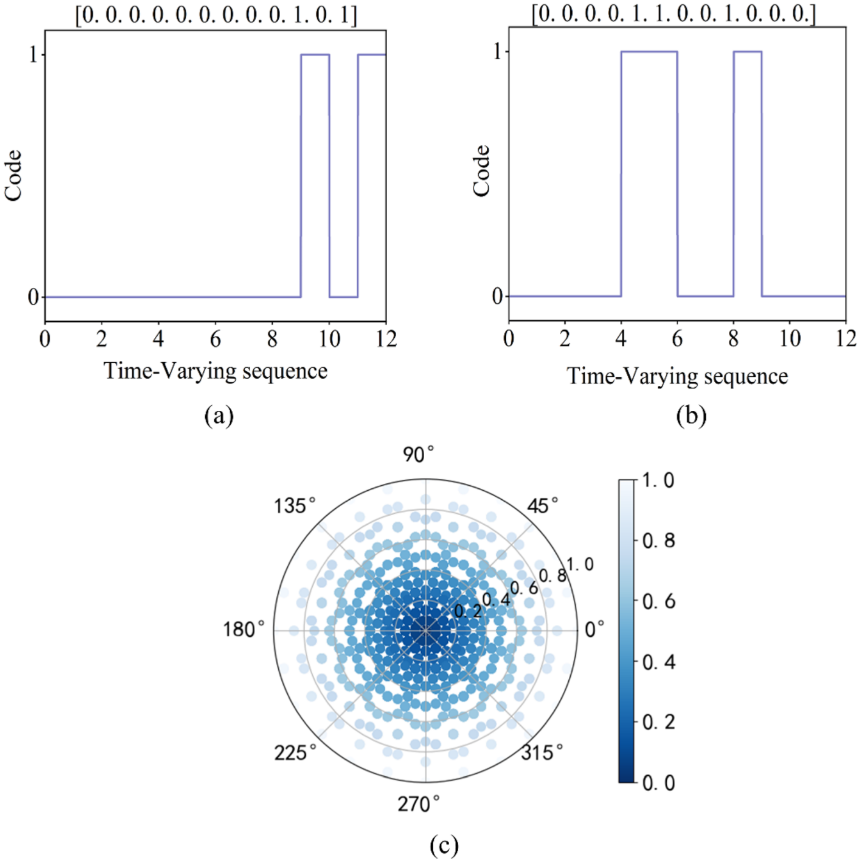

Fig. 7 (a and b) The binary codes for the 5th and 200th sequences with $L=12$. (c) Complex amplitude distribution at the -1st order harmonic.

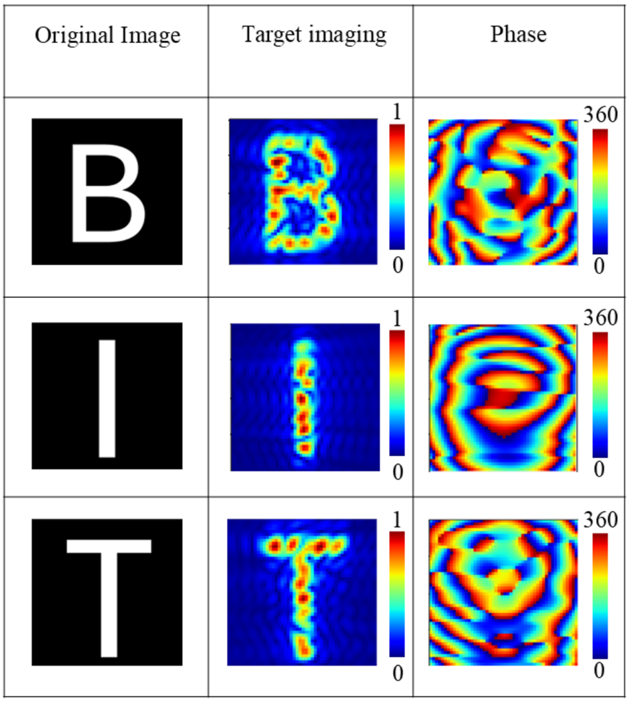

Fig. 8 Holographic imaging performance and phase distribution of 'B,' 'I,' and 'T' at the -1st harmonic of the GSRIS.

7.24 dB, respectively, indicating that the obtained holographic images have good quality. Based on the amplitude and phase distributions at the -1st order harmonic, the corresponding time-encoded sequences can be obtained from the amplitude and phase distribution database at the -1st order harmonic shown in Fig. 7(c). This result demonstrates that the proposed GSRIS can simultaneously generate multiple holographic images. Therefore, it can be concluded that the designed GSRIS can provide the amplitude and phase control required for holographic imaging, demonstrating the feasibility of the concept.

3.3. Practical aspects of design

Considering that the GSRIS proposed in this paper operates in the THz frequency band and different modulation techniques offer different modulation speed ranges in the THz frequency band, which can impact the system's performance and efficiency. Moreover, diodes are among the most commonly utilized technologies for applications in the gigahertz (GHz) range. However, owing to size limitations imposed by diodes on the minimum dimensions of each meta-atom, they are not suitable for applications at frequencies higher than GHz. Therefore, the electro-tuning of graphene facilitates the development of a rapid and reliable modulation scheme for implementing the proposed time-modulated encoding strategy. Furthermore, a GSRIS was successfully realized using an active radio frequency (RF) bias network, which enables independent addressing and biasing of each grid.

As modulation frequency of $f_0 = 3\text{GHz}$ was selected, as it falls within the practical range. Importantly, by considering the resolution of the terahertz detector, the resulting frequency harmonics can be effectively resolved. The primary challenge lies in selecting the appropriate modulation speed for the current signal system. In this paper, FPGA is employed as the processing module to apply the required time-modulated bias signal to GSRIS units. Furthermore, a review of existing technologies indicates the availability of several high-speed FPGAs capable of generating and designing time-modulated bias signals in the several gigahertz (GHz) range. Consequently, from this perspective, the design of the GSRIS is achievable.

While the results presented in this manuscript are based on full-wave EM simulations, we acknowledge that real-world implementation often presents challenges that may not be fully captured in simulations. As such, we have discussed some of the fabrication techniques and potential difficulties that may arise in the manufacturing process of the proposed graphene spatiotemporal reconfigurable intelligent surface (GSRIS).

The proposed GSRIS is primarily based on graphene, which has become increasingly feasible for fabrication using various methods such as chemical vapor deposition (CVD), laser-assisted chemical etching, and graphene oxide reduction. These techniques enable the production of high-quality graphene sheets that can be integrated with metamaterials or metasurfaces. The integration of graphene with a metasurface structure typically involves the following steps:

High-quality graphene can be synthesized on copper foils *via* CVD, followed by transfer onto a suitable substrate such as silicon or quartz. The metasurface structure, designed to manipulate EM waves at terahertz frequencies, is typically fabricated using photolithography or electron-beam lithography to create precise patterns on the substrate. *Graphene integration*: the graphene sheets are transferred onto the patterned metasurfaces. Techniques such as transfer printing or direct growth onto the surface can be used to ensure that the graphene layers are aligned with the metasurface structure. *Tuning the chemical potential*: to enable dynamic control of the chemical potential in graphene, devices such as field-effect transistors (FETs) or capacitive gating structures may be incorporated to modulate the electric field or voltage applied to graphene, thus adjusting its chemical potential.

While these fabrication techniques have seen success in laboratory environments, several challenges remain in their scaling up to real-world applications, particularly in the context of terahertz-frequency devices: the performance of the GSRIS heavily relies on the quality of graphene. Variations in graphene sheet quality, such as defects or non-uniformity in thickness, can affect the efficiency of polarization control and beam generation. Achieving uniform and high-quality graphene over large areas remains a significant challenge.

The metasurface must be patterned with nanometer-scale precision to effectively manipulate terahertz waves. Lithography techniques such as electron-beam lithography offer high resolution but are expensive and time-consuming. For large-scale production, alternative approaches such as nanoimprint lithography could be explored, although their scalability remains a concern. *Integration of components*: combining graphene with metasurfaces in a manner that enables seamless modulation of terahertz waves may involve challenges related to material compatibility, electrical contact, and interface quality between graphene and other materials. These integration challenges could affect the long-term stability and efficiency of the device. Because of to the high frequency and power levels involved in terahertz systems, managing heat dissipation in GSRIS devices may become a significant challenge. While the integration of graphene, known for its excellent thermal conductivity, could help alleviate this issue, the overall thermal performance of the device will need to be carefully evaluated.

4. Conclusion

In summary, we simulated a new graphene spatiotemporal reconfigurable intelligent surface (GSRIS) for dynamic terahertz polarization control, multi-beam generation, and holographic imaging. The proposed GSRIS offers strong tunability by applying different chemical potentials to graphene at 1.3 THz, enabling dynamic control of terahertz frequency EM waves. It is important to note that the number of beams and polarization states is not limited to those presented in this paper; they can generally be designed to accommodate different or more complex vector beam patterns. In this study, we demonstrated that terahertz polarization states can be controlled to generate up to four beams, each possessing a distinct polarization state while maintaining exceptional suppression of scattering below −25 dB in all directions. Finally, we showed that the GSRIS demonstrates high-quality terahertz holographic imaging at the -1st harmonic. The SNRs for the holographic images of the letters “B”, “I”, and “T” were found to be 7.65 dB, 7.55 dB, and 7.24 dB, respectively.

This technology holds great potential in future research, particularly in the development of adaptive terahertz systems for real-time polarization control and multi-beam generation. The ability to dynamically manipulate terahertz EM waves offers significant advances in imaging, sensing, and communication technologies. For instance, in 6G wireless communication, GSRISs can enable ultra-high-speed data transmission with tailored beamforming and secure communication channels by modulating the polarization state of terahertz waves. Furthermore, GSRIS-based systems could play a key role in intelligent sensing and imaging technologies, such as medical imaging, environmental monitoring, and security applications, by allowing for highly controlled, multi-dimensional beam patterns. Industrial applications can span from secure data encryption to adaptive beam control for radar systems and smart sensors. The reconfigurability and tunability of GSRISs make them a promising candidate for integration into next-generation communication and sensing infrastructures.

Data availability

The data that support the findings of this study are available from the corresponding author upon reasonable request.

Conflicts of interest

The authors declare that they have no known competing financial interests or personal relationships that could have appeared to influence the work reported in this paper.

Acknowledgements

This research was funded by the National Key R&D Program of China (grant no. 2022YFF0604801), the National Natural Science Foundation of China (grant no. 62271056, 62171186, and 62201037), the Beijing Natural Science Foundation of China-Haidian Original Innovation Joint Fund (grant no. L222042), and the 111 Project of China (grant no. B14010).

References

1 P. H. Siegel, Terahertz technology in biology and medicine, *IEEE Trans. Microwave Theory Tech.*, 2004, **52**(10), 2438–2447.
2 S. Nie and I. F. Akyildiz, Channel modeling and analysis of inter-small-satellite links in terahertz band space networks, *IEEE Trans. Commun. Syst.*, 2021, **69**(12), 8585–8599.
3 X. Wang, Z. Zhang, Y. Xu, L. Zhang, R. Yan and X. Chen, Real-time terahertz characterization of minor defects by the YOLOX-MSA network, *IEEE Trans. Instrum. Meas.*, 2022, **71**, 1–10.
4 C. K. Walker, *Terahertz Astronomy*, CRC Press, Boca Raton, 2015.
5 S. Helal, H. Sarieddeen, H. Dahrouj, T. Y. Al-Naffouri and M. S. Alouini, Signal processing and machine learning techniques for terahertz sensing: an overview, *IEEE Signal Process. Mag.*, 2022, **39**(5), 42–62.
6 Q. Wang, L. Xie and Y. Ying, Overview of imaging methods based on terahertz time-domain spectroscopy, *Appl. Spectrosc. Rev.*, 2022, **57**(3), 249–264.
7 H. Chen, H. Sarieddeen, T. Ballal, H. Wymeersch, M.-S. Alouini and T. Y. Al-Naffouri, A tutorial on terahertz-band localization for 6G communication systems, *IEEE Commun. Surv. Tutor.*, 2022, **24**(3), 1780–1815.
8 Y. Wei, L. Si, L. Dong, Q. Shen, T. Ma, H. Sun and X. Bao, A mid-IR tunable graphene metasurface for ultrasensitive molecular fingerprint retrieval and refractive index sensing, *J. Mater. Chem. C*, 2023, **11**(47), 16501–16508.
9 X. Pang, O. Ozolins, S. Jia, L. Zhang, R. Schatz, A. Udalcovs, V. Borovs, H. Hu, T. Morioka, Y. Sun, J. Chen, S. Lourdudoss, L. Oxenlowe, S. Popov and X. Yu, Bridging the terahertz gap: photonics-assisted free-space communications from the submillimeter-wave to the mid-infrared, *J. Lightwave Technol.*, 2022, **40**(10), 3149–3162.
10 P. Gopalan and B. Sensale-Rodriguez, 2D materials for terahertz modulation, *Adv. Opt. Mater.*, 2020, **8**(3), 1900550.
11 H. Zhang, L. Si, T. Ma, L. Dong, R. Niu, X. Bao, H. Sun and J. Ding, Triple-band terahertz chiral metasurface for spin-selective absorption and reflection phase manipulation, *Electronics*, 2022, **11**(24), 4195.
12 W. Xing, L. Si, L. Dong, H. Zhang, T. Ma, H. Sun, X. Bao and J. Ding, Rapid design of hybrid mechanism metasurface

with random coding for terahertz dual-band RCS reduction, *Opt. Express*, 2023, **31**(17), 28444–28458.

13 P. Tang, X. Zheng, T. Ma, G. Cheng, G. Wu, X. Bao, H. Sun, J. Ding and L. Si, Terahertz dual-band dual-polarization 3-Bit coding metasurface for multiple vortex beams generation, *Electronics*, 2023, **12**(8), 1868.

14 L. Dong, L. Si, H. Xu, Q. Shen, X. Lv, Y. Zhuang and Q. Zhang, Rapid customized design of a conformal optical transparent metamaterial absorber based on the circuit analog optimization method, *Opt. Express*, 2022, **30**(5), 8303–8316.

15 L. Si, Y. Liu, H. D. Lu, H. J. Sun, X. Lv and W. Zhu, Experimental realization of high transmittance THz 90° -bend waveguide using EMXT structure, *IEEE Photonics Technol. Lett.*, 2013, **25**(5), 519–522.

16 G. Cheng, L. Si, P. Tang, Y. Zhuang, H. Sun and J. Ding, Topology optimization of the azimuth-rotation-independent polarization conversion metasurface for bandwidth enhancement, *Opt. Express*, 2022, **30**, 41340–41349.

17 A. Samaha, J. Doumani, T. Kritzell, H. Xu, A. Baydin, P. M. Ajayan, M. Tahchi and J. Kono, Graphene terahertz devices for sensing and communication, *Small*, 2024, **2024**, 2401151.

18 *Graphene Production and Application*, ed S. Ameen, M. Akhtar and H. Shin, Intech Open, London, 2020.

19 A. Singh, M. Andrello, N. Thawdar and J. M. Jornet, Design and operation of a graphene-based plasmonic nano-antenna array for communication in the terahertz band, *IEEE J. Sel. Areas Commun.*, 2020, **38**(9), 2104–2117.

20 K. Yuan and L. Ye, Design and simulation of high-efficiency broadband terahertz graphene composite waveguide modulators, *IEEE J. Sel. Top. Quantum Electron.*, 2024, **30**(4), 1–9.

21 Y. Plotnik, M. Rechtsman, D. Song, M. Heinrich, J. Zeuner, S. Nolte, Y. Lumer, N. Malkova, J. Xu, A. Szaeit, Z. Chen and M. Segev, Observation of unconventional edge states in ‘photonic graphene, *Nat. Mater.*, 2014, **13**, 57–62.

22 A. K. Singh, E. S. Penev and B. I. Yakobson, Armchair or zigzag? A tool for characterizing graphene edge, *Comput. Phys. Commun.*, 2011, **182**(3), 804–807.

23 P. Ares and K. S. Novoselov, Recent advances in graphene and other 2D materials, *Nano Mater. Sci.*, 2022, **4**(1), 3–9.

24 Y. Cao, V. Fatemi, S. Fang, K. Watanabe, T. Taniguchi, E. Kaxiras and P. Jarillo-Herrero, Unconventional superconductivity in magic-angle graphene superlattices, *Nature*, 2018, **556**(7699), 43–50.

25 Y. Liu, X. Liu, X. Mu, T. Hou, J. Xu, M. D. Renzo and N. AI-Dhahir, Reconfigurable intelligent surfaces: principles and opportunities, *IEEE Commun. Surv. Tutor.*, 2021, **23**(3), 1546–1577.

26 N. Ashraf, T. Saeed, H. Taghvaee, S. Abadal, V. Vassiliou, C. Liaskos, A. Pitsillide and M. Lestas, Intelligent beam steering for wireless communication using programmable metasurfaces, *IEEE Trans. Intell. Transp. Syst.*, 2023, **24**(5), 4848–4861.

27 Y. Han, X. Li, W. Tang, S. Jin, Q. Cheng and T. J. Cui, Dual-polarized RIS-assisted mobile communications, *IEEE Trans. Wirel. Commun.*, 2022, **21**(1), 591–606.

28 Y. Zhuang, L. Si, H. Huang and T. Cai, Highly efficient Airy beam generator with high polarization purity by a receiving-transmitting metasurface, *Opt. Express*, 2024, **32**(18), 31325–31333.

29 L. Si, R. Niu, G. Cheng and W. Zhu, Experimental realization of a transmissive microwave metasurface for dual vector vortex beams generation, *Opt. Express*, 2024, **32**(8), 14892–14903.

30 G. Cheng, L. Si, Q. Shen, R. Niu, Q. Yuan, X. Bao, H. Sun and J. Ding, Transmissive pancharatnam-berry metasurfaces with stable amplitude and precise phase modulations using dartboard discretization configuration, *Opt. Express*, 2023, **31**(19), 30815–30831.

31 F. Faraz, Z. Zhang, Y. Huang, H. Fraz, T. U. R. Abbasi, X. Wang and W. Zhu, Bi-layer reflection-transmission dual-mode metasurface with flexible bandwidth control, *Adv. Opt. Mater.*, 2024, **12**(12), 232608.

32 R. Y. Wu, L. Zhang, L. Bao, L. Wu, Q. Ma, G. Bai, H. Wu and T. J. Cui, Digital metasurface with phase code and reflection-transmission amplitude code for flexible full-space electromagnetic manipulations, *Adv. Opt. Mater.*, 2019, **7**(8), 1801429.

33 L. G. Silva, L. C. Alexandre, P. Xiao and S. A. Cerqueira, RIS development and implementation in a mm-waves 5G-NR system toward 6G, *IEEE Wirel. Commun.*, 2024, **13**(3), 736–740.

34 L. M. Si, T. Jiang, K. Chang, T. Chen, X. Lv, L. Ran and H. Xin, Active microwave metamaterials incorporating ideal gain devices, *Materials*, 2011, **4**(1), 73–83.

35 X. Wu, Z. Li, Z. Zhang, X. Wang, L. Si and W. Zhu, Mechanically reconfigurable folded reflectarray antenna for variable near-field focusing, *IEEE Trans. Antennas Propag.*, 2023, **71**(12), 10038–10043.

36 E. Arbabi, A. Arbabi, S. Kamali, Y. Horie, M. Faraji-Dana and A. Faraon, MEMS-tunable dielectric metasurface lens, *Nat. Commun.*, 2018, **9**(1), 812.

37 C. Pan, H. Ren, K. Wang, J. Kolb, M. Elkashlan, M. Chen, M. Renzo, Y. Hao, J. Wang, A. Swindlehurst, X. Yu and L. Hanzo, Reconfigurable intelligent surfaces for 6G systems: principles, applications, and research directions, *IEEE Commun. Mag.*, 2021, **59**(6), 14–20.

38 L. Zhang and T. J. Cui, Space-time-coding digital metasurfaces: principles and applications, *Research*, 2021, **2021**, 9802673.

39 J. Y. Dai, J. Yang, W. Tang, M. Chen, J. Ke, Q. Cheng, S. Jin and T. J. Cui, Arbitrary manipulations of dual harmonics and their wave behaviors based on space-time-coding digital metasurface, *Appl. Phys. Rev.*, 2020, **7**(4), 041408.

40 D. L. Sounas and A. Andrea, Non-reciprocal photonics based on time modulation, *Nat. Photonics*, 2017, **11**(13), 774–783.

41 L. Zhang, X. Q. Chen, R. W. Shao, J. Y. Dai, Q. Cheng, G. Castaldi, V. Galdi and T. J. Cui, Breaking reciprocity with space-time-coding digital metasurfaces, *Adv. Mater.*, 2019, **31**(41), 1904069.

42 Q. Hu, W. Yang, J. Wang, X. Lu, J. Zhao, T. Jiang, K. Chen and Y. J. Feng, Dynamically generating diverse multi-beams with on-demand polarizations through space-time coding metasurface, *Adv. Opt. Mater.*, 2024, **12**(6), 2300093.

43 F. Yang, T. C. Tan, S. Prakash, A. Kumar, A. Ariando, R. Singh, N. Wang and P. Pitchappa, Reconfigurable wide-angle beam-steering terahertz metasurfaces based on vanadium dioxide, *Adv. Opt. Mater.*, 2024, **12**(9), 2002047.

44 H. Li, H. Xu, C. Zheng, J. Liu, J. Li, C. Song, J. Li, F. Yang, W. Shi, Y. Zhang, Y. Zhang and J. Yao, All-silicon diatomic terahertz metasurface with tailorable linear polarization states, *Adv. Opt. Mater.*, 2023, **11**(2), 2201960.

45 F. Ding, S. Zhong and S. I. Bozhevolnyi, Vanadium dioxide integrated metasurfaces with switchable functionalities at terahertz frequencies, *Adv. Opt. Mater.*, 2018, **6**(9), 1701204.

46 C. Caloz and Z. L. Deck-Léger, Spacetime metamaterials—part I: general concepts, *IEEE Trans. Antennas Propag.*, 2020, **68**(3), 1569–1582.

47 C. Caloz and Z. L. Deck-Léger, Spacetime metamaterials—part II: theory and applications, *IEEE Trans. Antennas Propag.*, 2020, **68**(3), 1583–1598.

48 P. C. Tang, L. M. Si, L. Dong, G. Wu, T. Ma, X. Bao and H. Sun, Tunable broadband terahertz graphene metasurface for complex-amplitude vortex beam generator and hologram, *Opt Laser. Technol.*, 2024, **175**, 110874.

49 W. Zhu, I. D. Rukhlenko, L. M. Si and M. Premaratne, Graphene-enabled tunability of optical fishnet metamaterial, *Appl. Phys. Lett.*, 2013, **102**(12), 121911.

50 Q. Hu, K. Chen, J. Zhao, S. Dong, T. Jiang and Y. J. Feng, On-demand dynamic polarization meta-transformer, *Laser Photonics Rev.*, 2023, **17**(1), 2200479.